Effect of post weld heat treatment on microstructure and mechanical properties of gas tungsten arc welded AA6061-T6 alloy

Firouz FADAEIFARD[1], Khamirul Amin MATORI[1,2], Farhad GARAVI[1],
Muath Al-FALAHI[1], Gholamreza Vahedi SARRIGANI[1]

1. Materials Synthesis and Characterization Laboratory, Institute of Advanced Technology,
Universiti Putra Malaysia, 43400 UPM Serdang, Selangor, Malaysia;
2. Department of Physics, Faculty of Science, Universiti Putra Malaysia, 43400 UPM Serdang, Selangor, Malaysia

Abstract: Double-V butt TIG welding process was performed on two plates of AA6061-T6 using ER5356 filler. The microstructure, mechanical and nanomechanical properties of the joint were evaluated in as-welded and after post weld heat treatment (PWHT) using XRD, FESEM, EBSD, nanoindentation and tensile tests. The results show that PWHT led to microstructural recovery of the heat affected zone (HAZ) in addition to the appearance of β-phase (Al_3Mg_2) at the grain boundaries of weld zone. The hardness (H_{nano}) in all zones increased after PWHT while the elastic modulus (E_{nano}) was improved from 69.93 GPa to 81 GPa in weld area. All results indicate that PWHT has created a homogenous microstructure in the weld zone in addition to outstanding improvement in mechanical properties for the weld zone which surpass the base metal.
Key words: AA6061-T6 alloy; ER5356; gas tungsten arc welding; post weld heat treatment; nanoindentation; microstructure

1 Introduction

Aluminum alloys have been increasingly applied in different industries, therefore, several research works on the manufacturing processes of these alloys have been developed over the time such as joining processes.

AA6061-T6 alloy is one variation of aluminum alloys, which is a heat treatable alloy that is used widely in shipbuilding, aerospace and automotive industries [1]. Despite the development in friction stir welding (FSW) as a solid state welding [2,3], fusing welding is still vastly applied for thick joint design. Furthermore, solid state joining such as FSW is not applicable for positions such as overhead, horizontal and vertical.

The main issue associated in welding AA6061-T6 aluminum alloy is the tendency of the weldment to overage which leads to deterioration in its mechanical properties. The high heat generated in the welding process and the resultant thermal cycle and cooling rate in parent metal lead to inhomogeneous heating and cooling in the surrounding area of the joint creating the so-called heat affected zone (HAZ). This can pose detrimental effects on the microstructure and consequently on the mechanical properties of AA6061-T6 weldment [4−7].

Totally, there are three main zones in the TIG-welded joint of AA6061-T6 which are investigated in this study.

1) The weld zone: This zone can include subzones with different microstructures depending on the number of welding passes.

2) The heat affected zone (HAZ): The HAZ can be divided into two subzones. The first zone is near to the weld pool, called HAZ1 in this work, and this zone can mostly experience the solution temperature 803−843 K (530−570 °C). Whereas, by decreasing the temperature toward the base metal, the second subzone appears that it is called HAZ2 in this work. This zone is exposed to the temperature under solution temperature and overaging that occurs at temperature of 373−573 K (100−300 °C) is the dominate experience. The famous reaction that occurs in HAZ2 is where the incoherent Mg_2Si (β) phase appears after permutation from semi coherent needles (β') and rods (β'') Mg and Si mixture as the following [1,4,7−9]:

GP-zones→β''→β'→β (Mg$_2$Si)

3) Base metal: The existence of zones and subzones with different microstructures in a confined area at small scale requires the implementation of specific characterization of each zone and subzone. One of the methods for mechanical characterization is the instrumented indentation that has been utilized to achieve local characterization of welded joints [7,10,11] as well as phases in metals and materials [12]. Recently, nanoindentation, which is an advanced method of indentation, has shown significant progress for measuring the local mechanical properties [13−16]. Some research works have been done on applying nanoindentation in measuring the mechanical properties of weld joints and this process has been known as nanomechanical characterization [17−19]. Until now, there is no remarkable work that is concerned about nanomechanical characterization for AA6061-T6 in TIG welding.

Oliver–Pharr (O&P) method in analyzing the nanoindentation tests results has been used effectively to determine the local nanomechanical properties of solids such as elastic modulus (E) and hardness (H). This method was based on analyzing the initial slope (S) of the unloading curve in the load−displacement curve [16].

Post weld heat treatment (PWHT) is applied in order to efficiently improve the mechanical and chemical properties of the fusion-welded joint by relieving the residual stresses and modifying the microstructure in the heat treatable alloys such as aluminum alloys [20−22]. For fusion welded AA6061-T6 alloy, some studies have done full T6 heat treatment as PWHT that includes solution and age hardening (artificial or natural) [20,22], while age hardening or different tempering were applied in others [21]. Consequently, different mechanical and microstructural properties were resulted by using these two different methods of PWHT. It is worth knowing that in the multi pass TIG welding of AA6061-T6 alloy, HAZ experiences the biggest microstructural deterioration due to the high heat input. By applying subsequent passes, the weldment is exposed to a temperature in the solution range then overaging range [4,5]. The HAZ gets worse by adding a new pass (new thermal cycle) in the joint design and, therefore, there should be more emphasis on applying post weld heat treatment (PWHT) to overcome the effect of the multi thermal cycles in AA6061-T6 alloy [23].

Furthermore, the filler metal (ER5356) plays a role in the microstructural alteration due to the emerging Al/Mg compounds in the weld zone under the influence of repeated thermal cycles during the subsequent passes [24−29]. It is, therefore, expected to have variations in the mechanical properties after each subsequent pass and after PWHT.

Accordingly, investigating and comparing the mechanical and nanomechanical properties of the weld zone before and after PWHT are highly important.

In this study, nanoindentation tests have been performed on the three main zones (weld zone, HAZ and base metal) in as-welded and after PWHT conditions at four welding passes, and their results have been utilized to calculate the hardness and elastic modulus for TIG double-V butt welded AA6061-T6 alloy. PWHT microstructures of weld zone and HAZ in as-welded and after PWHT conditions have been also investigated using optical microscopy, FESEM, EBSD and XRD.

2 Experimental

2.1 Welding and PWHT

In this study, an AA6061-T6 welded plate with thickness of 10 mm was used in this work. Table 1 shows the chemical compositions of the parent alloy and filler metal. The two plates were fabricated in butt joint design double-V with bevel angle of 80° and dimensions of 300 mm × 150 mm × 10 mm. The joint design (Fig. 1) was welded with ER5356 filler metal with diameter of 1.6 mm in 4 passes. Current of 200 A was applied in the first two passes and 160 A has been used in the third and fourth passes. Before performing the second pass, the back of weld was ground to remove probabilistic flaw of root pass. The macrostructure morphology of the welded joint is shown in Fig. 2. The welding specimens were separated in as-welded and PWHT samples for characterizations.

As for PWHT, the weldments were heated at 833 K (560 °C) for 1 h soaking time in an electric furnace, and then quenched in water at a temperature of 323 K (50 °C) followed by artificial aging at 448 K (175 °C) for 8 h soaking time and finally they were quenched in water at a temperature of 298 K (25 °C).

Table 1 Chemical compositions of materials (mass fraction, %)

Material	Si	Mg	Cu	Fe	Mn	Cr	Zn	Ti	Al
AA6061-T6	0.54	0.96	0.27	0.43	0.05	−	0.02	0.02	Bal.
ER5356	0.11	4.89	0.20	0.28	0.10	0.15	0.08	0.14	Bal.
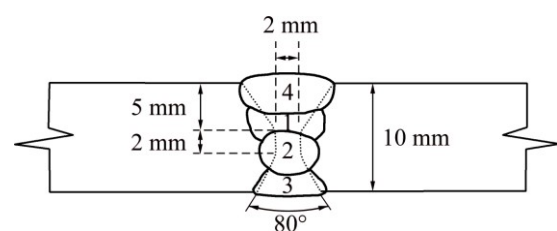
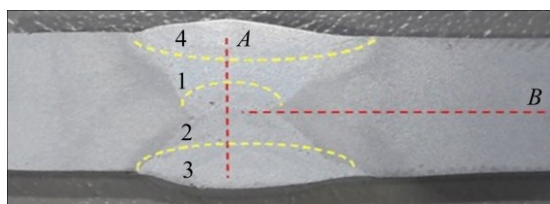**Fig. 1** Joint design and welding sequences

Fig. 2 Macrograph of weldment in as-welded condition

2.2 Microstructure and mechanical inspection

In order to study the microstructure, the welded joints samples (in as-welded and after PWHT conditions) were cut perpendicularly to the weld bead. After grinding and final polishing down to 1 μm using diamond paste, the samples were etched in Keller's reagent for 2 min. Lecia light microscope was used to ensure the appearance of the microstructure of weld zones in all samples, whereas FESEM (Nova NanoSEM 230) with EDS was used for microstructural analysis of all samples.

To identify the precipitation and phases, XRD analysis was carried out on the samples using Philips X'pert equipped with Cu K_{α} lamp with wavelength of 0.154 nm.

For further characterization of the microstructure of the welded joints, EBSD analyses were applied to studying the grain boundries and orientations. In order to prepare the sample for EBSD analysis, they were further polished to 0.5 μm using colloidal silica on VibroMet®2 vibratory polisher for 6 h. The EBSD analyses were performed using variable pressure SEM and data were acquired using the EDAX TEAM software.

The Vickers microhardness measurements were carried out on the samples in different zones on the cross-section perpendicular to weld direction using a square-base diamond pyramid indenter fixed on a microhardness tester at a load of 500 g at every 1 mm with a dwell time of 10 s.

Tensile tests were done at room temperature using a 100 kN Instron universal testing machine at fixed cross head speed of 2.0 mm/min. The number and dimensions of the samples used for tensile testing were selected in accordance with ISO 4136. The fractured surfaces were investigated using FESEM (Nova NanoSEM 230).

2.3 Nanoindentation

Nanoindentation tests were carried out using Hysitron© Triboindenter 750 Ubi system with Berkovich diamond tip. The results were then applied to calculating the hardness and the elastic modulus of the weldments. As for sample preparation, all samples were polished down to 1 μm with diamond paste followed by 0.5 colloidal silica. There were 2 measurement lines in each sample as shown in Fig. 2. Line A passes the weld joint

from top to bottom, while line B passes horizontally along HAZ, weld zone and base metal.

The applied load was fixed for all measurements at 2500 mN with loading and unloading time of 30 s and holding time of 10 s. The hardness and elastic modulus were obtained based on the difference in displacement for each point which is known as Oliver−Pharr method [16].

The unloading stiffness (S) is firstly determined by calculating the initial slope of the unloading curve and then applied to the following equation to obtain the non-constant indenter-surface contact area (A_c):

$$A_c = A\left(h - \varepsilon \frac{p}{s}\right) \tag{1}$$

where A is the area of the indenter, ε is the indenter's geometry constant which equals 0.75, and h is the total displacement in the test. Then, the hardness can be determined using the following equation:

$$H = \frac{p_{max}}{A_c} \tag{2}$$

where P_{max} refers to the peak load of the indentation. On the other hand, the reduced elastic modulus (E_r) can be determined using the following equation:

$$E_r = \frac{\sqrt{\pi}}{2} \frac{S}{\sqrt{A_c}} \tag{3}$$

The reduced elastic modulus which refers to the elastic deformation in both sample and indenter can also be expressed in the following equation:

$$E_r^{-1} = \frac{(1-v_i^2)}{E_i} \times \frac{(1-v_s^2)}{E_s} \tag{4}$$

where S refers to the contact stiffness determined from the unloading curve, E and v refer to the elastic modulus of workpiece and Poisson ratio, respectively. The subscripts i and s denote indenter and sample, respectively. In fact, Berkovich's diamond tip has elastic modulus of 1140 GPa and Poisson ratio of 0.07 while Poisson ratio for AA6061-T6 alloy is 0. 33.

3 Results and discussion

3.1 Microhardness (H_{micro}) and microstructure of weld zone and HAZ

Macrostructure of the weld metal and HAZ (including solution area−HAZ1 and overaging area−HAZ2) of AA6061-T6 TIG welded in as-welded condition are shown in Fig. 2. The sequence of welding passes was indicated in Fig. 1. There is no clear border between HAZ1 and HAZ2; however, the changes in microstructure were observed roughly in the middle

distance between fusion line and base metal which was also confirmed by H_{micro} measurement. Microhardness tests were done at cross section of weld in as-welded and PWHT samples and the results are illustrated in Fig. 3. As shown in Fig. 3(a), the highest hardness belongs to base metal whereas HAZ2 has the lowest hardness due to overaging of Mg_2Si [4,5] in as-welded sample. The difference in the hardness value between HAZ1 near to dilution line and the base metal is almost HV 20 whereas this difference between hardness in HAZ2 (the lowest value in as-weld sample) and in base metal is HV 60. By doing PWHT, the hardness in HAZ and base metal shows a uniform trend and the lowest value of hardness belongs to weld zone as shown in Fig. 3(b). The last pass has the lowest hardness and the first pass shows the highest amount in as-welded sample. PWHT changed the hardness in weld zone and increased it to HV 81 and made uniform hardness profile in comparison with the as-welded sample.

Figure 4 shows the dendritic microstructure which forms by the high solidification and cooling rate [30,31] in the center of pass 4 in weld zone. This microstructure was reported in pervious works which used Mg-rich filler metal [24−26].

However, emersion of second phase, in worm shape, in the first, second and third welding passes, can be seen in Fig. 5(a) that presents the microstructure of the second pass of welding, whereas, this microstructure is nearly repeated in the first and third passes as well. Figure 5(b) presents the microstructure of the first pass, while the first pass was undergone 3 welding thermal cycles of the second pass to the fourth pass; it is observed that the second phases are connected to each other in some areas and are shaped like grain boundaries. The zones which are indicated by P in these 2 figures show the poropsity in weld zone. Due to relatively high diffusion of hydrogen in melted aluminum, the exsistence of porosity in weld zone is unavoidable in fusion welding. However, these prosities should be greater than 700 μm to overcome the surface tension of the solid/liquid interface. Additionally, a low solidification rate is needed to allow the gas bubble coalescence and reach mentioned value (700 μm). Nonetheless, the high solidification rate in TIG welding does not allow the hydrogen to get big enough and exit from welding pool [32].

The worm shape appeared phase (A in Fig. 5) which emerged from dendritic structure was investigated by EDS and the result presented in Fig. 6 shows the presence of Mg and Al in this phase.

Consequently, by doing XRD characterization for weld zone (Fig. 7), the formation of Al−Mg compounds was confirmed by the existence of Al_3Mg_2 (β-phase) intermetallic compound in the weld area. The appearance of β-phase is a result of welding thermal cycle, which imposed tempering to each previous welded passes;
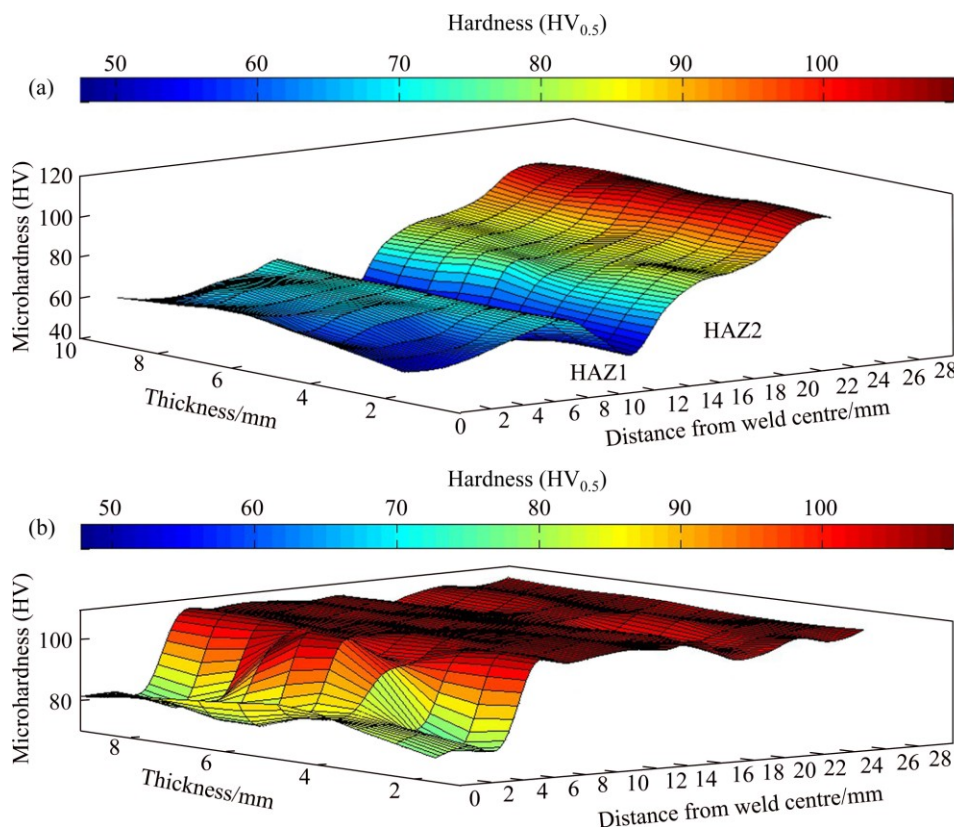

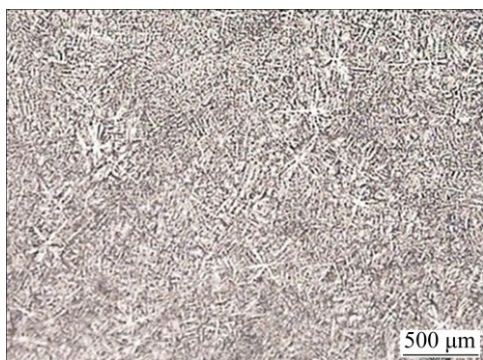**Fig. 3** Distribution of microhardness: (a) As-welded sample; (b) After PWHT
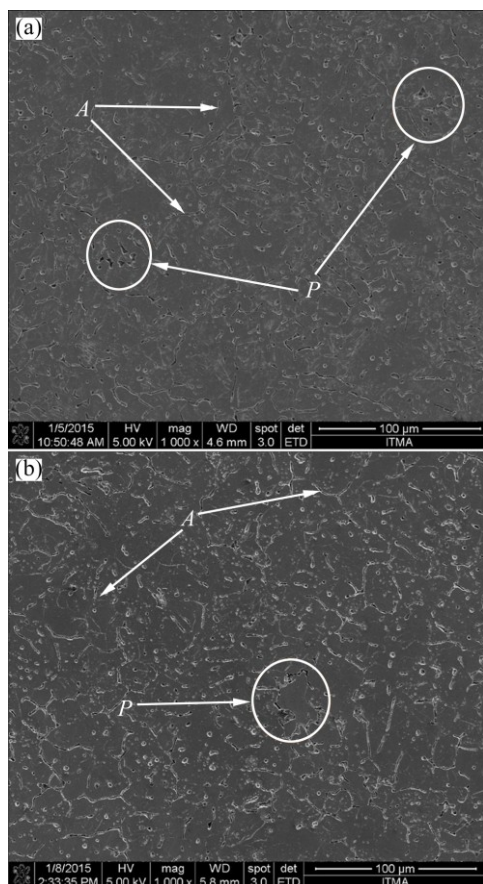
Fig. 4 Microstructure of last pass (pass 4)

Fig. 5 FE-SEM images of weld zone in as-welded sample: (a) Second pass; (b) First pass

Fig. 6 EDS spectrum of point A in Fig. 5(a)
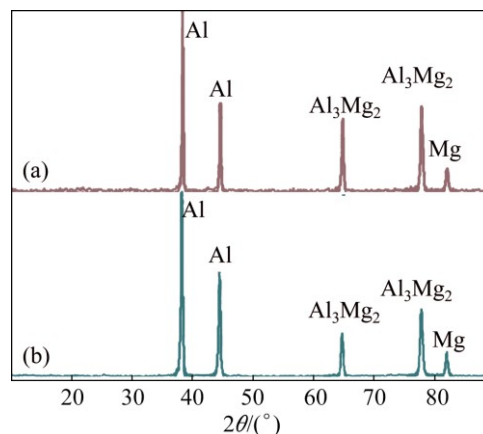
Fig. 7 XRD patterns of weld zone: (a) As-weld; (b) PWHT

however, due to the high cooling rate and insufficient time in welding, interconnected network of grain boundary is not formed. The heat input of welding and applied thermal cycle for each pass not only can influence the microstructure of base metal (AA6061-T6) but can change the microstructure and morphology of previous welded passes of ER5356 by changing β-phase spreading in matrix [27−29]. The effect of heating is noticeable in Al_3Mg_2 distribution in 5356 aluminum alloy [28,33,34] and consequently any changes in the distribution and redistribution of β-phase can affect the mechanical and metallurgical properties [28,34−36].
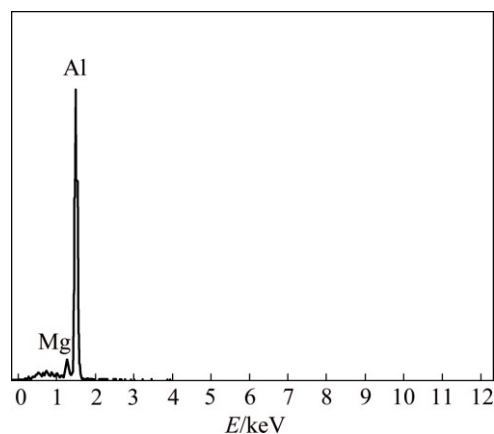
Indeed, in the Al−Mg binary phase diagram, the maximum solubility of Mg in Al is 18.6% at the eutectic temperature of 723 K (450 °C) and 5356 aluminum alloy, which has 4.9% Mg, can include α-phase (Al) and β-phase (Al_3Mg_2) at room temperature till about 473 K (200 °C). The β-phase Al_3Mg_2 intermetallic compound entirely dissolves into the Al matrix when the temperature is higher than 723 K (450 °C) (at eutectic line). Therefore, the peak temperature 833 K of PWHT in solution (560 °C)) is enough for the Al_3Mg_2 to completely dissolve into the matrix [37,38]. However, this alloy can encounter the formation of α and β phases by doing age hardening at 448 K (175 °C), whereas the β-phase forms at grain boundaries. The presence of β-phase (Al_3Mg_2) at grain boundaries is in agreement with findings of CHOI et al [34] and SCAMANS et al [39,40]. This means that although ER5356 is not categorized as a heat treatable alloy, post weld heat treatment for the weldment has changed the entire microstructure of weld zone where β-phase (Al_3Mg_2) formed as an interconnected grain boundary in all four passes of welding; however, there are some β-phase particles inside each grain. This uniformity of

microstructure can confirm the hardness homogeneity of weld zone in PWHT sample as shown in Fig. 3(b). Figure 8 shows equiaxed grains which were formed in the first pass after PWHT. The EDS spectrum of A in Fig. 8(a) matched with that of as-welded sample as presented in Fig. 6.
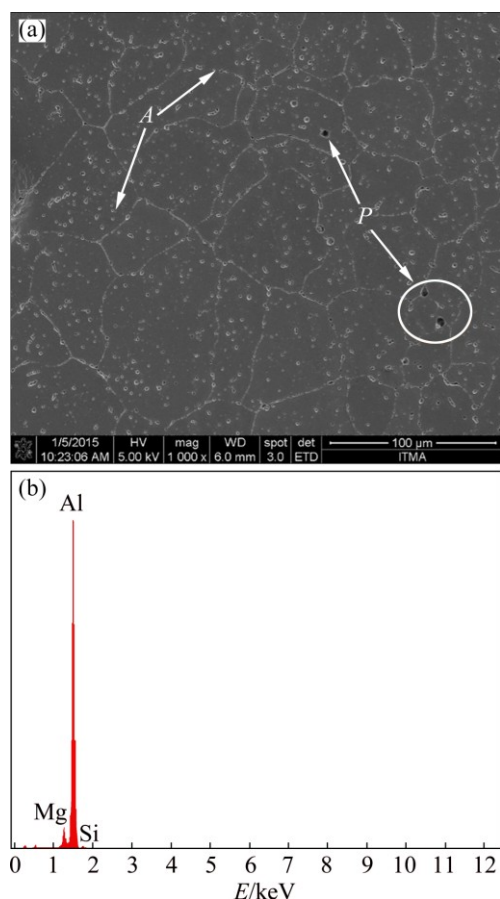
Fig. 8 FE-SEM microstructure (a) of weld zone after PWHT (pass 1) and EDS spectrum (b) of point A in (a)

As mentioned, the first pass has capability to create higher amount of Al_3Mg_2 due to the thermal cycle of the 2nd , 3rd and 4th passes. However, the exposure time to heat is not enough to complete emerging process for Al_3Mg_2. The presence of this phase at grain boundaries can be completed by applying longer time in age hardening of PWHT. This difference can be seen in Fig. 9 which displays higher magnification of the first pass in as-welded (Fig. 9(a)) and PWHT (Fig. 9(b)) conditions.

The variations in microstructure in the HAZ before and after heat treatment are different from the weld zone as already mentioned in the introduction. The HAZ in as-welded sample has two subzones: HAZ1 which is near to the weld zone and HAZ2 which is close to base metal. The solution was experienced by HAZ1 whereas over aging occurred in HAZ2 (also shows lower hardness). Figure 10(a) shows thicker grain boundaries
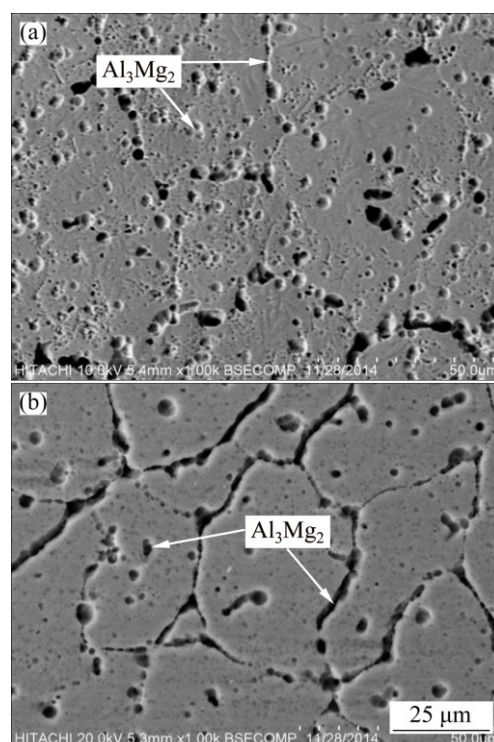

Fig. 9 Microstructures of first welding pass: (a) As-weld; (b) PWHT

(immigrated precipitations) due to solution of precipitation (denoted as A in Fig. 10(a)) in HAZ1 [5] while in HAZ2 thinner grain boundaries and bigger second phases (precipitation coarsening) [5] occur (denoted as B in Fig. 10(b)). The transformation from β'' to β' and finally β (Mg_2Si) precipitates occur by an extent and repeated thermal cycle of each welding pass. These findings are consistent with the previous works done by other researchers [4,5]. The EDS of B in Fig. 10(b) confirmed Mg, Al and Si in second phases (B) in Fig. 10(b) whereas in coarser phases (C) the mass fraction of Si was further valued.

Figure 11 shows the EBSD images of HAZ2. The colouring shows the crystallographic orientations of grains with an orientation code triangle being displayed below Figs. 11(a) and (b) whereas the guide of misorientation of grain boundaries is indicated by lines in different colours. There are some low angle grain boundaries (thinner black line) which are referred to precipitation coarsening and segregation to nucleate new grains [41,42] due to high heat input of welding in Fig. 11(a). However, the PWHT for HAZ of TIG welded AA6061-T6 alloy removed and eliminated low angle boundaries inside the grains via solution and reprecipitation in aging temperature as shown in Fig. 11(b). The grain boundary misorientation can affect the microstructure and subsequently mechanical properties. Therefore, the changes in high angle misorientation fraction from 0.497 to 0.903 due to
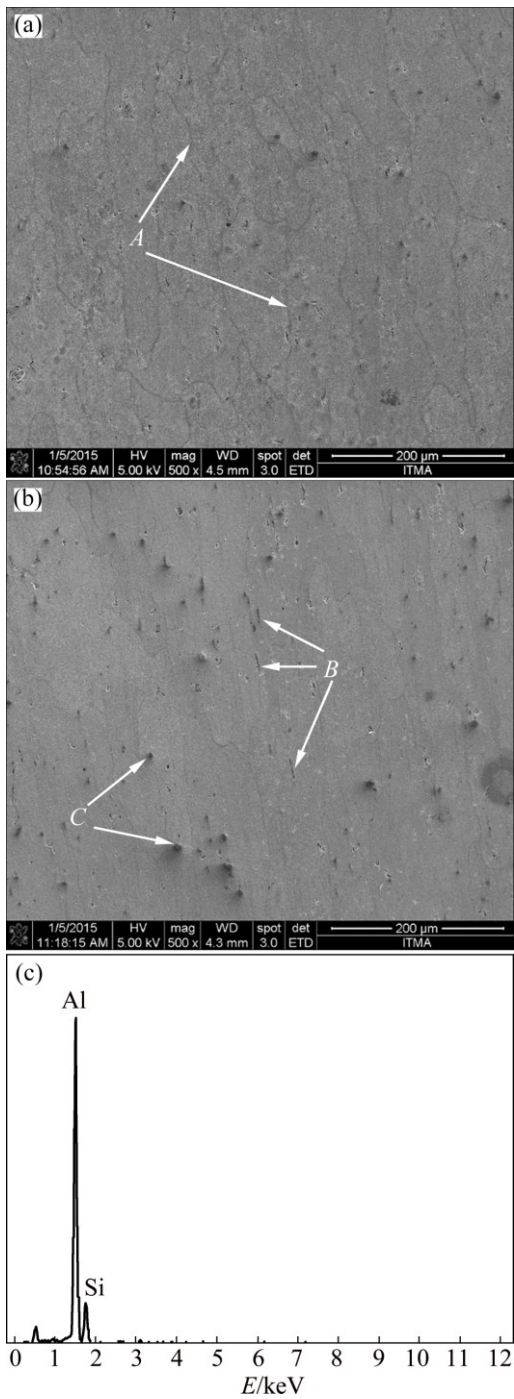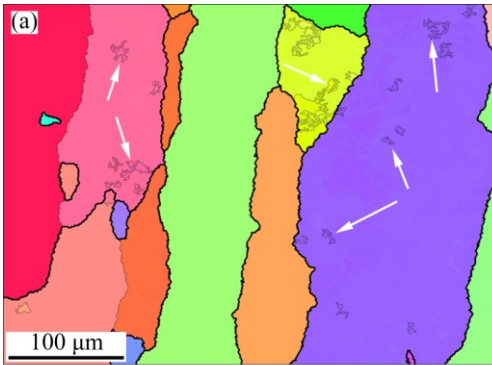
Fig. 10 FE-SEM images of HAZ in as-welded sample: (a) HAZ1; (b) HAZ2; (c) EDS spectrum of point *B* in Fig. 10(b)

Fig. 11 EBSD orientation images and their corresponding boundary map: (a) HAZ2 of as-welded sample; (b) After PWHT

PWHT (Fig. 11) have significant role in mechanical and nanomechanical properties of HAZ. The comparison between Figs. 11(a) and (b) indicates the uniform microstructure of HAZ after PWHT.
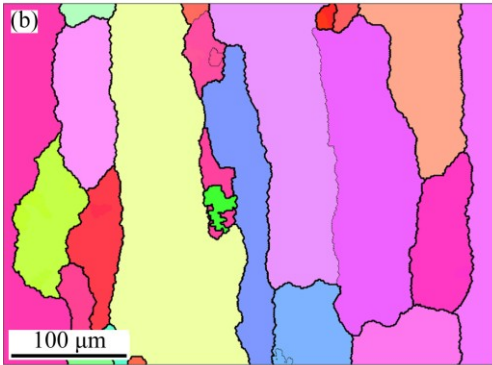
Microstructural changes in weld zone and HAZ and the existence of secondary phases in as-welded and PWHT samples can affect the local mechanical properties of each zone and pass in as-welded and PWHT samples [7].

3.2 Fractoghraphy

Tensile tests of as-welded and PWHT samples were performed at room temperature and the results are presented in Table 2. Increase of 54% was observed in yield strength (70.3 to 130.8 MPa) whereas ultimate tensile strength (UTS) was improved from 137.7 MPa to 204.4 MPa (50%). These improvements in yield and ultimate strengths are the outcome of PWHT [43]. However, the plastic strain was significantly decreased in

PWHT sample (3.6% elongation compared with 13% elongation). The failure location in as-welded sample was in HAZ2 (overaging area) while the necking was observed during tensile test. However, in the PWHT sample, failing occurred in weld region and the noticable necking was not seen in this sample. Both failings happened in hardness minima of as-welded and PWHT weldments.

Table 2 Results of tensile tests

Sample	UTS/MPa	Yield strength/MPa	Elastic modulus/GPa	Elongation/%
As-welded	137.7	70.3	60.3	13
PWHT	204.4	130.8	76.9	3.6

Figure 12 shows the fracture surfaces of as-welded sample with low and high magnifications. As can be seen, the morphologies of fractures include a great number of fine dimples which are distributed uniformly on the fracture surface. A ductile fracture was resulted in as-welded sample accompanied with a good plastic deformation.

Due to the less elongation in PWHT, the brittle fracture or brittle−ductile fracture was expected for this sample. Figure 13(a) exhibits a fracture surface with dominant brittle features including cleavage facets (*A*) and shallow and big dimple-shape features (*B*) which introduce a brittle−ductile fracture [44,45]. However, in shallow dimples that indicated in Fig. 13(b), microcracks can be observed. EDS shows the Al−Mg composition in these area. This may prove that during the tensile test, microcracks form in the β-phase (Al_3Mg_2) connected networks at grain boundaries of weld region due to lower resistance to deformation compared with matrix [33] whereas the better plasticity of aluminum in matrix stopped the propagation of these micocracks.

3.3 Nanoindentation hardness (H_{nano}) and elastic modulus (E_{nano})

The nanoindentation tests were performed along lines *A* and *B* (Fig. 2) in both as-welded and PWHT samples. The precipitation size in T6 condition has been mostly reported around 50 nm [1,8−9]. Therefore, the Berkovich nanoindenter which has 6 μm in dimension in
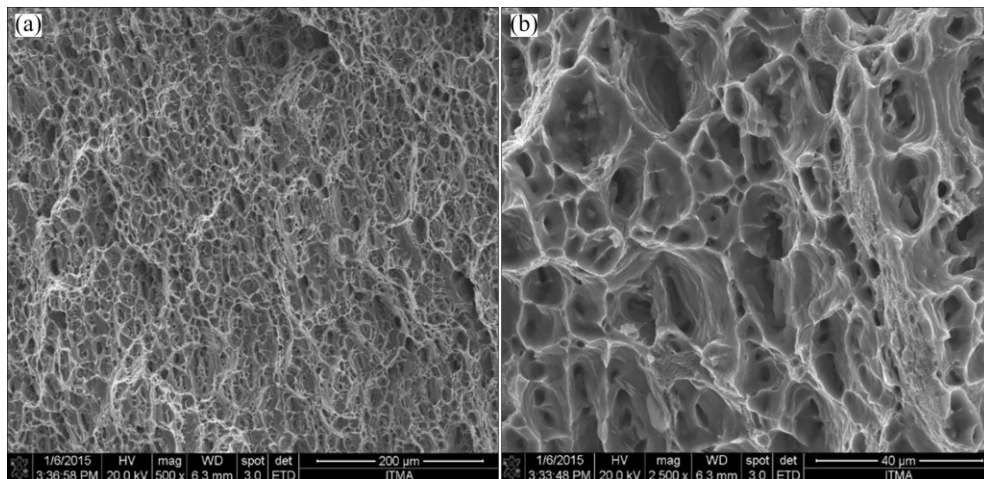

**Fig. 12** Fractographs of as-welded sample: (a) Low magnification; (b) High magnification
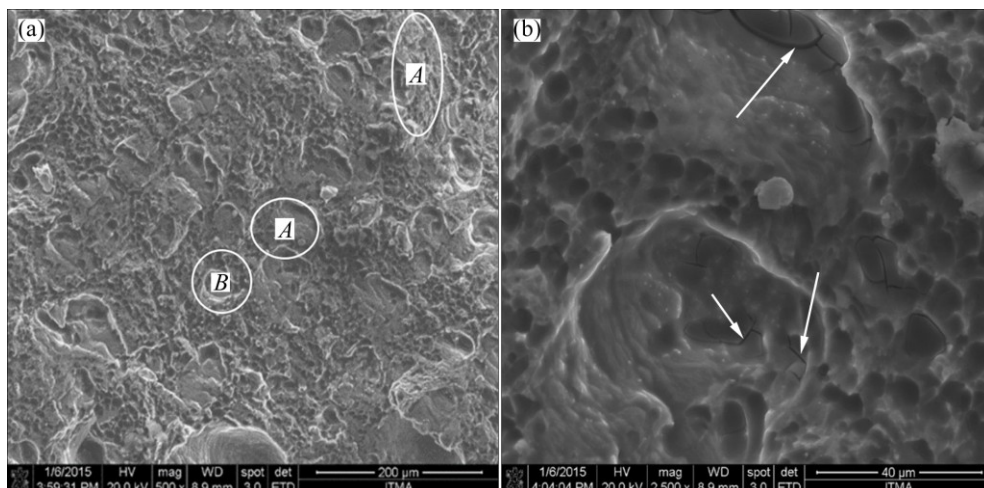
Fig. 13 Fractographs of PWHT sample: (a) Low magnification; (b) High magnification

base and 1 μm in height [14] cannot disturb the nanoindentation results significantly. However, in overaging condition, the size of precipitation has been reported more than 250 nm [1,8,9] and in solution condition, the thickness of boundaries can affect the nanoindentation data. For the purpose of minimizing the error caused by the contact between Berkovich indenter and metal precipitation during nanoindentation tests, at least 16 tests were done in each zone and the non-consistent values were then removed. After that, Figs. 14−17 were provided and illustrated.
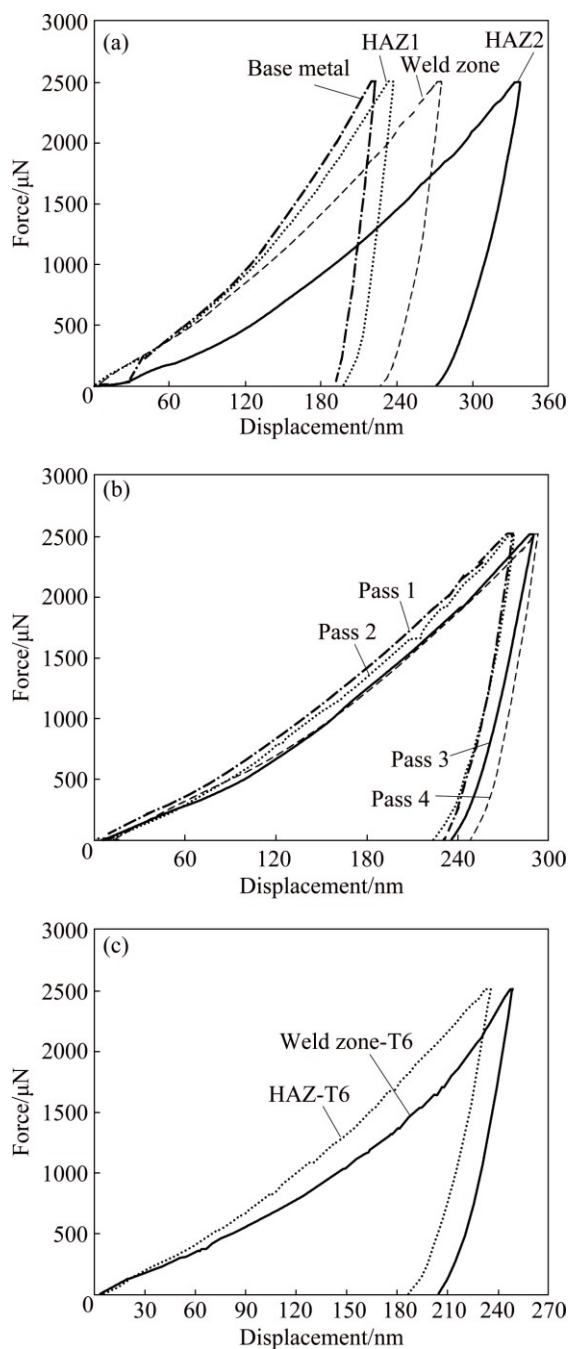
Fig. 14 *P*−*h* curve of nanoindentation tests: (a) Along as-welded sample; (b) Along welding passes in as-welded sample; (c) PWHT sample
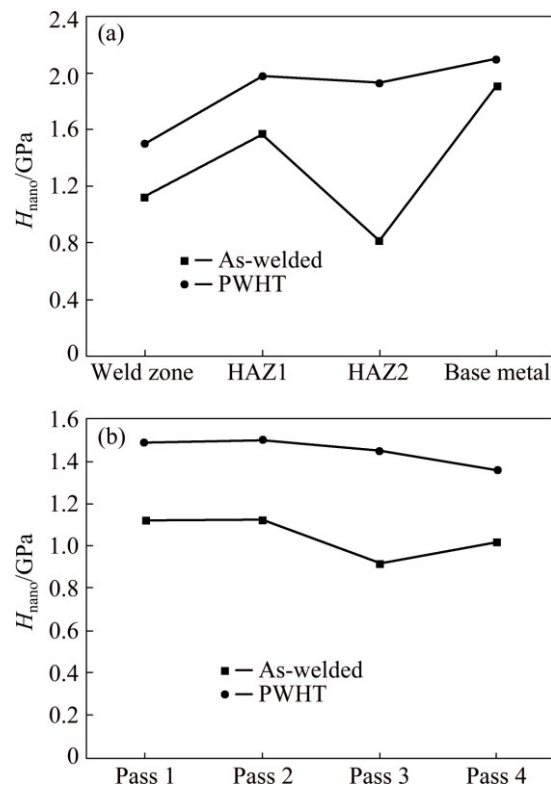
Fig. 15 H_{nano} profile: (a) In weldment along line *B* of Fig. 2 (as-weld and PWHT); (b) Along welding passes (as-welded and PWHT)
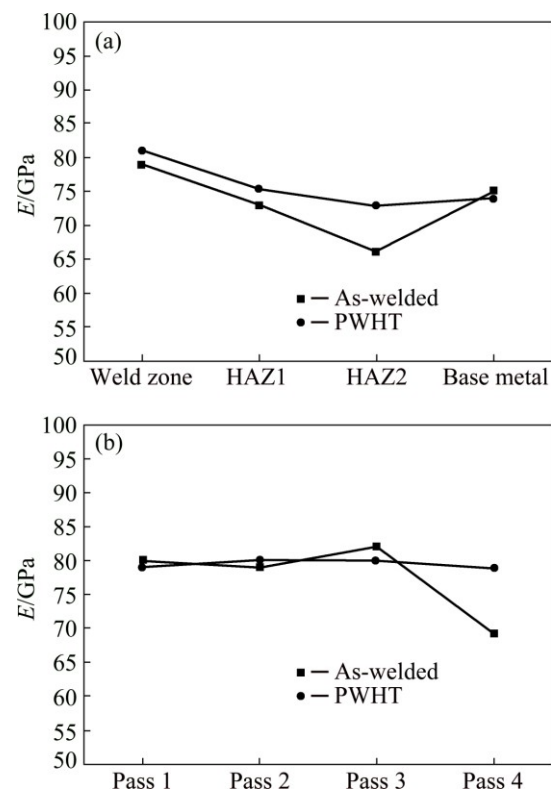
Fig. 16 Elastic modulus profile: (a) In weldment along line *B* of Fig. 2 (as-weld and PWHT); (b) Along welding passes (as-welded and PWHT)

Fig. 17 Cross section of pile-up in HAZ2

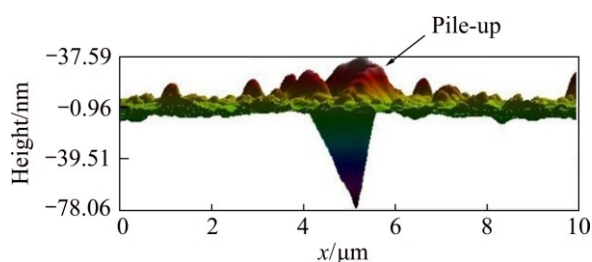In Fig. 14(a), the results of the nanoindentation tests which were carried out along line *B* in Fig. 2 that includes weld zone, HAZ1, HAZ2 and the base metal of as-welded sample are displayed in force−displacement (*P*−*h*) curve. Different zones of weldment show different displacement when the same force of 2500 μN is applied. In fact, the displacement was increased due to lower surface resistance (hardness) of each investigated zone in moving to left side of the curves. The highest displacement, which belongs to HAZ2, shows significant difference in base metal which experienced the lowest displacement. However, the total displacements of base metal and HAZ1 present a close trend. Although, the total displacement in base metal is about 8 % less than HAZ1 (around 15 nm) but the effective displacements of both, which resulted from interruption in the displacement axis and unloading curve [14,16], show smaller difference around 5% (less than 10 nm). Even though total displacements in some cases have insignificant difference, the base and foundation for differences in the local mechanical properties (H_{nano} and *E*) comes from the unloading stiffness, *S* [14−16]. It can be seen in the following that H_{nano} variation for this 2 zones is more than 20 %. The displacement curve of the weld zone is located between the displacements of HAZ1 and base metal.

Figure 14(b) shows the *P*−*h* curves for different welded passes in the weld zone of as-welded samples. The minimum displacement belongs to the first and second passes which experienced higher tempering and thermal cycling of welding process. However, the highest displacement was for the last pass which has a complete dendritic microstructure unlike other passes where *β*-phase (Al_3Mg_2) presents which have lower displacement.

Nanoindentation tests were carried out on PWHT sample and the results are presented in Fig. 14. It is clear in Fig. 14(c) that the HAZ of as-welded sample after performing PWHT shows a suitable sameness in total displacement and unloading stiffness compared with base metal in Fig. 14(a). After PWHT, *P*−*h* curves for all four passes of welding have almost become similar. The H_{nano} that is obtained from *P*−*h* curves in Fig. 14 is shown in Fig. 15.

The changes in the H_{nano} results along line *B* (Fig. 2) in as-welded and PWHT samples are shown in Fig. 15(a). The lowest H_{nano} in as-welded sample was in HAZ2 whereas in the lowest H_{nano} in PWHT was in weld zone. The non-uniform sketch of as-welded sample is related to dissolution of precipitations in the HAZ1 and overaging of precipitation in the HAZ2. Indeed, this variation in H_{nano} is ascribed to the microstructural transformation of *β″* to *β′* and finally *β* (Mg_2Si) precipitates. When HAZ1 presented 1.6 GPa H_{nano} in value, base metal showed 1.91 GPa. After applying PWHT, the H_{nano} changed from the value 0.816 GPa in HAZ2 of as-welded to 1.93 GPa in PWHT sample. The main reason for hardness variation in AA6061-T6 is backing to precipitation size and distribution [1,7−9].

Figure 15(b) shows the H_{nano} of the weld zone. The highest hardness values in the weld zone of as-welded sample is equal to 1.12 GPa while after PWHT and the formation of the equiaxed grains the H_{nano} shows a noticeable rise to 1.5 GPa. Different chemical composition of weld zone which produced by ER5356 is the main reason correlated to variation of H_{nano} in weld zone compared with HAZ and base metal.

The results of H_{nano} show a similar trend in comparison to the H_{micro} results, although in H_{micro} characterization data in HAZ2 and weld zone are closer in comparison to the H_{nano} of HAZ2 and weld zone.

Figure 16 shows the results of E_{nano} in as-welded and PWHT samples along line *B* (Fig. 2). The HAZ2 has elastic modulus of 66.51 GPa, which is the lowest, whereas the maximum *E* belongs to base metal having a value of 74.52 GPa due to their different composition and microstructure in weld zone and base metal. As it is indicated in Fig. 16(a), the solution zone (HAZ1) presents higher elastic modulus compared with the overaging zone (HAZ2). This indicates the role of homogeneousness of microstructure in elastic properties of materials and elastic modulus [20,46−48]. In fact, inhomogeneous and dissimilar arrangement of precipitation in these two zones can evince different plastic deformation for applying each nanoindentor and any changes in plastic deformation during loading and unloading of nanoindentation can result different elastic response [49]. The other fusion welding can impose residual stress in the vicinity of weld zone [50] and presence of stress demonstrates the significant strain in that area. Effect of pre-strain on the elastic modulus has proved by ABDEL-KARIM [48]. Therefore, the difference in elastic modulus of HAZ and base metal is associated to the influence of residual stress on the HAZ while, in PWHT, similarity in E_{nano} was resulted by terminating residual stress.

The elastic modulus of each pass in as-welded and PWHT conditions of TIG welded AA6061 alloy is shown

in Fig. 16(b). It can be seen that pass 4, which has dendritic microstructure, has the lowest value in elastic modulus of 69.93 GP. However, in PWHT sample the similarity of elastic modulus in each pass can be seen to reach 81 GPa.

The importance of the contact area (A_c) for estimating E and H is clear from the equations used to obtain the H_{nano} and E_{nano}. However, the contact area is influenced by the so-called phenomenon of pile-up or sink-in. When pile-up refers to the projecting material around the indent, sink-in is the immersion of the material surrounding the indent as a result of the indenter vertical movement [14,15,46,47]. The relation between mechanical properties, such as creep, tensile strength, compression strength, hardness, residual stress and elastic modulus which affected by pile-up and sink-in phenomena have been discussed in numerous works [14,15]. In this project, pile-up has been observed due to the low strain hardening tendency of AA6061-T6 alloy which indicates the high plastic deformation in the workpiece [47]. Pile-up formation, which is inevitable in AA6061-T6 alloy, can affect the results by making an error in the actual A_c and consequently overestimating of E_{nano} [46,47]. Figure 17 shows the effect of the nanoindenter in HAZ2 of as-welded samples. Pile-up can be seen clearly in the cross section view in Fig. 17. The height of the pile-up in base metal and PWHT samples is lower than that in HAZ1 and HAZ2.

Since the failure of as-welded sample occurred in HAZ2, by comparing E_{nano} (65.91 GPa) and elastic modulus (60.3 GPa) in Table 2, there are less than 10% overestimating. However, in PWHT, there is almost 20% difference for these two values in weld zones (failing location). The elastic modulus of AA6061-T6 alloy is almost 65 GPa resulting from tensile test. The indentation stress is a complex mixture of tension, compression and shear in indented area whereas the tenile test is done in only tention condition. Due to the comperesive effect of indenter, the elastic modulus which resulted from indentation characterization has been emphasized to bulk modulus instead of elastic modulus by CHICOT et al [50] and AMBRIZ et al [7]. However, it has been trying to minimize the shear and compression effect by using minor rate of force (μN) in nanoindentation characterization and unloading elastic analyzing. Anyhow, the difference in E_{nano}, either elastic modulus or bulk modulus, is an indicative factor for changes of mechanical properties in each zone of weldment.

4 Conclusions

1) β-phase (Al_3Mg_2) at grain boundary was resulted from the transformation from dendritic microstructure to equiaxed microstructure as a result of PWHT in weld zone.

2) In the solution zone (HAZ1) of AA6061-T6 alloy, the grain boundaries are thick, whereas in overaging zone (HAZ2), the grain boundaries are thin but the secondary phases (coarsening precipitation), which form low angle boudaries in grains, are bigger. However, the low angle grain boundaries in HAZ2 was vanished after PWHT.

3) The UTS and yield strength in PWHT increased whereas the elongation decreased. The fracture locations were in HAZ2 (overaging area) and weld zone in as-welded sample and PWHT sample, respectively. While the fracture surface of as-welded sample showed a ductile feature, PWHT sample had brittle/ductile surface.

4) The lowest H_{nano} value in as-welded sample belongs to HAZ2 while in PWHT sample it is in the weld zone. Overall, PWHT samples show better uniformity and higher H_{nano}.

5) The value of nanoindentation elastic modulus (E_{nano}) and the obtained elastic modulus of tensile test in oveaging area of AA6061-T6 alloy showed relatively high similarity. In PWHT, there is 20% difference in elastic modulus of nanoindentation test and tensile test of fracture location in weld zone.

6) The composition can influence the E_{nano} (comparing weld zone and base metal) when the E_{nano} can be effected by microstructure (comparing HAZ1 and HAZ2).

7) Uniform hardness was achieved by doing PWHT, which can outcome the homogenous microstructure and relieve the residual stress.

References

[1] MAISONNETTE D, SUERY M, NELIASA D, CHAUDET P, EPICIER T. Effects of heat treatments on the microstructure and mechanical properties of a 6061 aluminium alloy [J]. Materials Science and Engineering A, 2011, 528: 2718−2724.

[2] MISHRA R S, MA Y Z. Friction stir welding and processing [J]. Materials Science and Engineering: R, 2005, 50: 1−78.

[3] FADAEIFARD F, MATORI K A, TOOZANDEHJANI M, DAUD A R, ARIFFIN M K, OTHMAN N I, GHARAVI F, OSTOVAN F. Influence of rotational speed on mechanical properties of friction stir lap welded 6061-T6 Al alloy [J]. Transactions of Nonferrous Metals Society of China, 2014, 24: 1004−1011.

[4] AMBRIZ R R, BARRERA G, GARCÍA R, LÓPEZ V H. The microstructure and mechanical strength of Al-6061-T6 GMA welds obtained with the modified indirect electric arc joint [J]. Materials &

Design, 2010, 31: 2978−2986.

[5]   AMBRIZ R R, BARRERA G, GARCÍA R , LÓPEZ V H. Effect of the weld thermal cycles of the modified indirect electric arc on the mechanical properties of the AA6061-T6 alloy [J]. Welding International, 2010, 24: 321−328 .

[6]   KUMAR A, SUNDARRAJAN S. Effect of welding parameters on mechanical properties and optimization of pulsed TIG welding of Al−Mg−Si alloy [J]. The International Journal of Advanced Manufacturing Technology, 2009, 42: 118−125.

[7]   AMBRIZ R R, CHICOT D, BENSEDDIQ N, MESMACQUE G, de La TORRE S D. Local mechanical properties of the 6061-T6 aluminium weld using micro-traction and instrumented indentation [J]. Eurpean Journal of Mechanic A−Solid, 2011, 30: 307−315 .

[8]   GUPTA A K, LLOYD D J, COURT S A. Precipitation hardening processes in an Al−0.4%Mg−1.3%Si−0.25%Fe aluminum alloy [J]. Materals Science and Engineering A, 2001, 301: 140−146.

[9]   EDWARDS G A, STILLER K, DUNLOP G L, COUPER M J. The precipitation sequence in Al−Mg−Si alloys [J]. Acta Materialia ,1998, 46: 3893−3904.

[10] JANG J, SON D, LEE Y H, CHOI Y, KWON D. Assessing welding residual stress in A335 P12 steel welds before and after stress-relaxation annealing through instrumented indentation technique [J]. Scripta Materialia, 2003, 48: 743−748 .

[11] HUBER N, HEERENS J. On the effect of a general residual stress state on indentation and hardness testing [J]. Acta Materialia, 2008, 56: 6205−6213.

[12] ZUPANIC F. Microindentation as a complementary method for phase identification [J]. Metals and Materials International, 2011, 17: 865−871.

[13] RAM H R A, KOPPAD P G, KASHYAP K T. Nanoindentation studies on MWCNT/aluminum alloy 6061 nanocomposites [J]. Materials Science and Engineering A, 2013, 559: 920−923.

[14] LUCCA D A, HERRMANN K, KLOPFSTEIN M J. Nanoindentation: Measuring methods and applications [J]. CIRP Annals–Manufcturing Technology, 2010, 59: 803−819.

[15] FISCHER-CRIPPS A C. Critical review of analysis and interpretation of nanoindentation test data [J]. Surface and Coatings Technology, 2006, 200: 4153−4165.

[16] OLIVER W C, PHARR G M. An improved technique for determining hardness and elastic modulus using load and displacement sensing indentation experiments [J]. Journal of Materials Research, 1992, 7: 1564−1583.

[17] KOUMOULOS E P, CHARITIDIS C A, DANIOLOS N M, PANTELIS D I. Nanomechanical properties of friction stir welded AA6082-T6 aluminum alloy [J]. Materials Science and Engineering B, 2011, 176: 1585−1589.

[18] CHARITIDIS C A, DRAGATOGIANNIS D A, KOUMOULOS E P, KARTSONAKIS I A. Residual stress and deformation mechanism of friction stir welded aluminum alloys by nanoindentation [J]. Materials Science and Engineering A, 2012, 540: 226−234 .

[19] CABIBBO M, FORCELLESE A, ELMEHTEDI M, SIMONCINI M. Double side friction stir welding of AA6082 sheets: Microstructure and nanoindentation characterization [J]. Materials Science and Engineering A, 2014, 590: 209−217.

[20] ZHU Z Y, DENG C Y, WANG Y, YANG Z W, DING J K, WANG D P. Effect of post weld heat treatment on the microstructure and corrosion behavior of AA2219 aluminum alloy joints welded by variable polarity tungsten inert gas welding [J]. Materials & Design, 2015, 65: 1075−1082.

[21] NIKSERESHT Z, KARIMZADEH F , GOLOZAR M A, HEIDARBEIGY M. Effect of heat treatment on microstructure and corrosion behavior of Al6061 alloy weldment [J]. Materials & Design, 2010, 31: 2643−2648.

[22] AHMAD R, BAKAR M A. Effect of a post-weld heat treatment on the mechanical and microstructure properties of AA6061 joints welded by the gas metal arc welding cold metal transfer method [J]. Materials & Design, 2011, 32: 5120−5126.

[23] MYHR O R, FJAR H G, MARIOARA C D. Modelling of the microstructure and strength evolution in Al−Mg−Si alloys during multistage thermal processing [J]. Acta Materialia, 2004, 52: 4997−5008.

[24] YAN S, CHEN H, ZHU Z, GOU G. Hybrid laser-metal inert gas welding of Al−Mg−Si alloy joints: Microstructure and mechanical properties [J]. Materials & Design, 2014, 61: 160−167.

[25] HADADZADEH A, GHAZNAVI M M, KOKABI A H. The effect of gas tungsten arc welding and pulsed-gas tungsten arc welding processes' parameters on the heat affected zone-softening behavior of strain-hardened Al−6.7Mg alloy [J]. Materials & Design, 2014, 55: 335−342 .

[26] BABU N K, TALARI M K, PAN D, SUN Z, WEI J, SIVAPRASAD K. Microstructural characterization and grain refinement of AA6082 gas tungsten arc welds by scandium modified fillers [J]. Materials Chemistry and Physics, 2012, 137: 543−551.

[27] SAAD G, FAYEK S A, FAWZY A, SOLIMAN N H, NASSR E. Work hardening characteristics of gamma-ray irradiated Al-5356 alloy [J].   Materials Science and Engineering A, 2014, 607: 132−137.

[28] SAAD G, FAYEK S A, FAWZY A, SOLIMAN N H , NASSR E. Serrated flow and work hardening characteristics of Al-5356 alloy [J]. Journal of Alloys and Compounds, 2010, 502: 139−146 .

[29] BALASUBRAMANIAN V, RAVISANKAR V, REDDY G M. Effect of pulsed current welding on fatigue behavior of high strength aluminium alloy joints [J]. Materials & Design, 2008, 29: 492−500.

[30] GANAHA T, PEARCE B P, KERR H W. Grain structures in aluminum alloy GTA welds [J]. Metallurgical Transactions A, 1980, 11: 1351−1359 .

[31] KOU S, LE Y. Welding parameters and the grain structure of weld metal — A thermodynamic consideration [J]. Metallurgical Transactions A, 1986, 19: 1075−1082 .

[32] AMBRIZ R R,   JARAMILLO D. Mechanical behavior of precipitation hardened aluminum alloys welds [C]//Light Metal Alloys Applications. InTech, 2014: DOI: 10.5772/58418.

[33] LIU C Y, JING R, WANG Q, ZHANG B, JIA Y Z, MA M Z, LIU R P. Fabrication of Al/Al$_3$Mg$_2$ composite by vacuum annealing and accumulative roll-bonding process [J]. Materials Science and Engineering A, 2012, 558: 510−516 .

[34] CHOI D H, AHN B W, QUESNEL D J, JUNG S B. Behavior of b phase (Al$_3$Mg$_2$) in AA 5083 during friction stir welding [J]. Intermetallics, 2013, 35: 120−127.

[35] SCUDINO S, SPERLING S, SAKALIYSKA M, THOMAS C, FEUERBACHER M, KIM K B, EHRENBERG H, ECKERT J. Phase transformations in mechanically milled and annealed single-phase b-Al$_3$Mg$_2$ [J]. Acta Materialia, 2008, 56:1136−1143.

[36] GOLOVIN I S, MIKHAYLOVSKAYA A V, SINNING H R. Role of the b-phase in grain boundary and dislocation anelasticity in binary Al−Mg alloys [J]. Journal of Alloys and Compounds, 2013, 577: 622−632.

[37] KOGTENKOVA O A, PROTASOVA S G, MAZILKIN A A, STRAUMAL B B, ZIE PCZEPPE T, BARETZKY B. Heat effect of grain boundary wetting in Al−Mg alloys [J]. Journal of Materials Science, 2012, 47: 8367−8671 .

[38] LUO C, LIANG W, CHEN Z, ZHANG J, CHI C, YANGC F. Effect of high temperature annealing and subsequent hot rolling on microstructural evolution at the bond-interface of Al/Mg/Al alloy laminated composites [J]. Materials Characterization, 2013, 84: 34−40.

[39] SCAMANS G M, REHAL A S. Electron metallography of the aluminium-water vapour reaction and its relevance to stress-

corrosion susceptibility [J]. Journal of Materials Science, 1979, 14: 2459−2470.

[40] SCAMANS G M, HOLROYD N J H, TUCK C D S. The role of magnesium segregation in the intergranular stress corrosion cracking of aluminium alloys [J]. Corrosion Science, 1977, 27: 329−347.

[41] LIU L, NAKAYAMA H, FUKUMOTO S, YAMAMOTO A, TSUBAKINO H. Microscopic observations of friction stir welded 6061 aluminum alloy [J]. Materials Transactions, 2004, 45: 288−291.

[42] SUHUDDIN U F H R, MIRONOV S, SATO Y S, KOKAWA H. Grain structure and texture evolution during friction stir welding of thin 6016 aluminum alloy sheets [J]. Materials Science and Engineering A, 2010, 527: 1962−1969.

[43] FAHIMPOUR V, SADRNEZHAAD S K, KARIMZADEH F. Microstructure and mechanical property change during FSW and GTAW of Al6061 alloy [J]. Metallurgical and Materials Transactions A, 2013, 44: 2187−2195.

[44] DING J K, WANG D P, WANG Y, DU H. Effect of post weld heat treatment on properties of variable polarity TIG welded AA2219 aluminium alloy joints [J]. Transactions of Nonferrous Metals Society of China, 2014, 24: 1307−1316.

[45] QUAN L I, WU A P, ZHAO Y, WANG G Q, YAN D Y, WU H Q.

Fracture behavior of double-pass TIG welded 2219-T8 aluminum alloy joints under transverse tensile test [J]. Transactions of Nonferrous Metals Society of China, 2015, 25: 1794−1803.

[46] LI X, BHUSHAN B. A review of nanoindentation continuous stiffness measurement technique and its applications [J]. Materials Characterization, 2002, 48: 11−36.

[47] BOLSHAKOV A, PHARR G M. Influence of pile-up on the measurement of mechanical   properties by load and depth sensing instruments [J]. Journal of Materials Research, 1998, 13: 1049−1058.

[48] ABDEL-KARIM M. Effect of elastic modulus variation during plastic deformation on uniaxial and multiaxial ratchetting simulations [J]. European Journal of Mechanics - A/Solids, 2011, 30: 11−21.

[49] JAMES M N, HUGHES D J, HATTINGH D G, MILLS G, WEBSTER P J. Residual stress and strain in MIG butt welds in 5083-H321 aluminium: As-welded and fatigue cycled [J]. International Journal of Fatigue, 2009, 31: 28−40.

[50] CHICOT D, ROUDET F, ZAOUI A, LOUIS G, LEPINGLE V. Influence of visco-elasto-plastic properties of magnetite on the elastic modulus: Multicyclic indentation and theoretical studies [J]. Materials Chemistry and Physics, 2010, 119: 75−81.

后续焊缝热处理对气体保护钨极电弧焊
AA6061-T6 合金显微组织和力学性能的影响

Firouz FADAEIFARD[1], Khamirul Amin MATORI[1,2], Farhad GARAVI[1],

Muath Al-FALAHI[1], Gholamreza Vahedi SARRIGANI[1]

1. Materials Synthesis and Characterization Laboratory, Institute of Advanced Technology,

Universiti Putra Malaysia, 43400 UPM Serdang, Selangor, Malaysia;

2. Department of Physics, Faculty of Science, Universiti Putra Malaysia,

43400 UPM Serdang, Selangor, Malaysia

摘　要：采用 ER5356 焊料对 AA6061-T6 合金板材进行双 V 坡口气体保护钨极焊接。采用 XRD、FESEM、EBSD、纳米压痕和拉伸测试研究焊接后及后续焊缝热处理后焊接接头的显微组织、力学性能和纳米力学性能。结果表明，后续焊缝热处理可使热影响区的显微组织恢复，并在焊缝区的晶界上形成 β 相(Al_3Mg_2)。经后续焊缝热处理后，所有区域的硬度均增加，而焊缝区的弹性模量从 69.93 GPa 增加至 81 GPa。经后续焊缝热处理后，焊接区的显微组织均匀，与基体合金相比，力学性能得到提高。

关键词：AA6061-T6 铝合金；ER5356 焊料；气体保护钨极电弧焊；后续焊缝热处理；纳米压痕；显微组织

(Edited by Yun-bin HE)